Heriot-Watt University
Research Gateway

Multi-target two-photon dual-comb LiDAR

Citation for published version:
Wright, H, Nelmes, AJM, Weston, NJ & Reid, DT 2023, 'Multi-target two-photon dual-comb LiDAR', *Optics Express*, vol. 31, no. 14, pp. 22497-22506. https://doi.org/10.1364/OE.490052

Digital Object Identifier (DOI):
10.1364/OE.490052

Link:
Link to publication record in Heriot-Watt Research Portal

Document Version:
Publisher's PDF, also known as Version of record

Published In:
Optics Express

General rights
Copyright for the publications made accessible via Heriot-Watt Research Portal is retained by the author(s) and / or other copyright owners and it is a condition of accessing these publications that users recognise and abide by the legal requirements associated with these rights.

Take down policy
Heriot-Watt University has made every reasonable effort to ensure that the content in Heriot-Watt Research Portal complies with UK legislation. If you believe that the public display of this file breaches copyright please contact open.access@hw.ac.uk providing details, and we will remove access to the work immediately and investigate your claim.

Download date: 14. May. 2025

Research Article Vol. 31, No. 14 / 3 Jul 2023 / Optics Express 22497
Optics EXPRESS

Multi-target two-photon dual-comb LiDAR

HOLLIE WRIGHT,[1,*] ALEXANDER J. M. NELMES,[1] NICK J. WESTON,[2] AND DERRYCK T. REID[1]

[1]Scottish Universities Physics Alliance (SUPA), Institute of Photonics and Quantum Sciences, School of Engineering and Physical Sciences, Heriot-Watt University, Edinburgh EH14 4AS, UK
[2]Renishaw Plc, Edinburgh EH14 4AP, UK
[*]H.Wright@hw.ac.uk

Abstract: By substituting two-photon cross-correlation in a wide-bandgap photodiode for the coherent gating conventionally used in dual-comb ranging, two-photon dual-comb LiDAR exchanges data-intensive interferometric acquisition for a single time-stamp from which an absolute distance can be inferred. Here, we report the application of two-photon dual-comb LiDAR to obtain real-time ranging to three independent targets with only a single silicon-photodiode detector. We show precisions of 197–255 nm (2 seconds averaging time) for static targets, and real-time simultaneous ranging to three dynamic targets driven by independent sinusoidal, saw-tooth and square waveforms. Finally, we demonstrate multi-target ranging to three points on a rigid body to provide simultaneous pitch and yaw angular measurements with precisions of 27.1 arcsec (130 µrad) on a 25 mm baseline.

Published by Optica Publishing Group under the terms of the Creative Commons Attribution 4.0 License. Further distribution of this work must maintain attribution to the author(s) and the published article's title, journal citation, and DOI.

1. Introduction

Dual-comb ranging (DCR), first reported by Coddington, *et al.* in 2009 [1], employs pulses from a probe comb to sample an unknown distance, and pulses from a local oscillator (LO) comb to coherently gate the returning probe pulses and obtain an absolute range measurement. The probe and LO combs are arranged with a small repetition frequency difference (Δf_{rep}), yielding interferograms which repeat at rate of Δf_{rep}. Interferometric DCR offers exceptional precision [2,3], but it is data intensive, requires tightly locked frequency combs, and is typically not amenable to real-time distance extraction. For some applications it is recognized that interferometric precision is excessive, and that sufficient precision (sub-µm) can be obtained by utilizing only the non-interferometric time-of-flight (TOF) component of the measurement. Despite this simplification, the same interferometric signal is often still collected, normally requiring a high-speed digitizer and sampling speeds >100 MSa/s. This is followed by *post-hoc* distance extraction, either in the spectral domain using windowing and Fourier transforming [4–6], or in the time domain by fitting an envelope to localize the center of the interferogram [7–11]. In principle, such a TOF measurement removes the need to lock the combs' carrier-envelope offset frequencies (f_{CEO}), but in practice, the use of free-running combs can allow the interferogram carrier frequency to drift towards DC, making envelope extraction difficult and degrading the distance measurement.

Recently, we introduced a new TOF approach – two-photon dual-comb LiDAR [12] – which shares characteristics with other cross-correlation-based dual-comb methods [13,14] but has a uniquely simple implementation that replaces the linear coherent detection conventionally used in DCR with the direct detection of two-photon cross-correlations in a wide-bandgap photodiode [15]. Detailed in [12], two-photon dual-comb LiDAR uses cross-correlations between the LO pulses and the target and reference probe pulses as the start and stop inputs to a fast electronic timer (see Section 2), allowing TOF measurements with a simple time-stamp data collection.

#490052 https://doi.org/10.1364/OE.490052
Journal © 2023 Received 20 Mar 2023; revised 25 May 2023; accepted 13 Jun 2023; published 21 Jun 2023

Optics EXPRESS

Replacing the high-bandwidth digitizer with the fast electronic timer represents a significant reduction in the equipment costs and the data burden. The simplicity of the data collection allows the distance to be calculated on-the-fly.

Our original demonstration achieved an instantaneous precision of 17.8 μm for 250 μs sampling intervals, and showed dynamic measurements at a few Hz, with real-time distance reporting and no limit on the acquisition duration. We now describe the extension of two-photon dual-comb LiDAR to enable simultaneous ranging to multiple targets using a single silicon-photodiode detector. No degradation in measurement performance is observed when extending from a single target to three targets, and we demonstrate simultaneous ranging to three dynamic targets driven by independent sinusoidal, saw-tooth and square waveforms.

Our multi-target sensing approach enables ranging to three points on a rigid body to provide simultaneous range and pose (pitch and yaw angle) measurements. To date, there are limited examples of dual-comb measurements of a target angle [5,16]; most optical angle measurements are based on either interferometry or autocollimation [17–21]. However, multi-target DCR offers the unique advantage that it simultaneously measures angle and absolute range. Examples of dual-comb angle sensing in the literature report measurement precisions between 5 and 90 arcsec at kHz update rates when measuring angle ranges <400 arcsec [5,16]. We demonstrate angular measurements over ranges up to 4000 arcsec with precisions between 23.8 and 70.0 arcsec.

2. Two-photon dual-comb LiDAR for simultaneous ranging to multiple targets

2.1. Dual-comb sources and metrology system

The probe and LO combs were SESAM-modelocked Er:fiber lasers, the designs of which have been reported previously [12] and which were constructed from polarization-maintaining (PM) fibers, except for a short free-space region for tuning the repetition frequency, f_{rep}. Both oscillators provided pulses with repetition frequencies of $f_{rep} \approx 78.98$ MHz, implying the LiDAR system had a non-ambiguity range (NAR) of 1.9 m. The combs had optical spectra centered at 1555 nm (probe) and 1552 nm (LO), and full-width at half maximum (FWHM) bandwidths of 6.2 nm (probe) and 4.8 nm (LO). The average optical power of each comb oscillator was 1 mW, and these powers were increased using two-stage Er:doped fiber amplifiers (EDFAs) to 41 mW (probe) and 12 mW (LO). During ranging, the repetition frequencies of the probe and LO combs were independently locked to enforce a measurement rate of $\Delta f_{rep} = 1$ kHz. In-loop power spectral density measurements of the f_{rep}-locking error signals from 1 Hz – 1 MHz implied a probe-comb phase noise of 140 mrad, which corresponds to a repetition frequency deviation of 22.3 mHz. The LO comb phase noise was 22.3 mrad, which corresponds to a repetition frequency deviation of 3.8 mHz.

The two-photon dual-comb LiDAR scheme for ranging to three targets is shown in Fig. 1(a). Pulses from the probe comb pass through quarter- and half-wave plates, which arrange them into p-polarizations which are transmitted at polarizing beam splitter PBS1. A wedge with one face aligned perpendicular to the beam path reflects 10% of the beam to act as a reference (R) signal. A diffractive optical element (DOE; Holo-Or TS-031-G-Y-A) splits the remaining power in the probe beam into three nominally equal components, distributed between the zeroth and $\pm 1^{st}$ order diffracted beams. Each of the three beams have ~12 mW optical power and are returned by an independent retroreflector (*T1–T3*) and recombined with the others at the DOE, similar to the method described in [16]. Each of the three beams is diffracted into three on the second pass through the DOE, leaving 12 mW of power in the recombined beam. A second pass through the quarter-wave plate arranges the reference and target reflections into s-polarizations, allowing them to be reflected at PBS1 and PBS2. The LO pulses are similarly conditioned into p-polarizations and are transmitted at PBS2, and in this way they are combined, orthogonally polarized, with the probe reflections to ensure they cannot optically interfere. A short focal length aspheric lens focuses the combined beam onto a silicon avalanche photodiode (APD). The

Optics EXPRESS

output is low-pass filtered at ~$f_{rep}/2$ to yield a sequence of four two-photon cross-correlations, one for the reference and one for each target. This signal is amplified and passed through a Schmitt trigger to transform each cross-correlation into a digital 3.3 V pulse suitable as a start / stop trigger for an electronic timer. A representative cross-correlation and corresponding Schmitt trigger output are shown in Fig. 1(b).

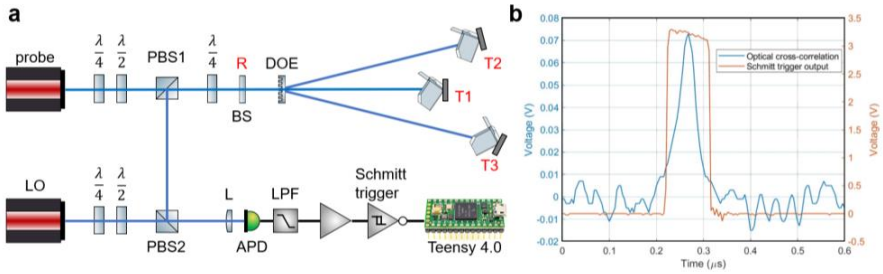

Fig. 1. (a) Two-photon dual-comb LiDAR scheme with three retroreflecting targets. PBS: polarizing beam splitter; R: reference; DOE: diffractive optical element; T: target; L: lens; APD: avalanche photodetector; LPF: low-pass filter. (b) Representative two-photon cross correlation (blue, FWHM 41 ns) and corresponding output from the Schmitt trigger (FWHM 90 ns).

The output of the Schmitt trigger is sent to the digital input of an Arduino Teensy 4.0 microcontroller, which is configured to count its internal central processing unit (CPU) cycles until an interrupt signal is detected on a preselected pin. When a rising edge is detected, the CPU cycle count is sent to the serial port, and the count is reset. In this way, the timing gaps between consecutive cross-correlations are recorded with 1.67 ns resolution, limited by the CPU clock frequency of 600 MHz. Figure 2(a) shows an example oscilloscope trace of the cross-correlation signal over approximately three measurement cycles. The pattern of a reference cross-correlation followed by three target cross-correlations is repeated at a rate equal to Δf_{rep}. Annotations on the figure illustrate the repeated timing interval τ_{1-4}, where τ_1 is the interval between the reference and the first target cross-correlation; τ_2 and τ_3 are the timing intervals between the three target cross-correlations; and τ_4 is the timing interval between the third target cross-correlation and the next reference cross-correlation. An example of raw data collected from the serial port is shown in Fig. 2(b) and is color coded to match the annotations in Fig. 2(a). The data presented in Fig. 2(a) and 2(b) were collected separately so the values do not correspond; the figures are provided to aid visualization of the measurement concept only.

The measurements present on the serial bus can be acquired in real-time by MATLAB or in the Arduino integrated development environment (IDE). These integer counts of the CPU cycles can be used to provide the absolute optical path lengths between the reference and each target optic according to:

$$d_i = \frac{v_g}{2f_{rep,pr}} \frac{\sum_{j=1}^{i} \tau_j}{(\tau_1 + \tau_2 + \tau_3 + \tau_4)}, \tag{1}$$

where v_g is the group velocity of the pulses and $f_{rep,pr}$ is the repetition frequency of the probe comb. In practice, we approximate v_g as being the vacuum speed of light, c, however an exact calculation requires the correct temperature- and humidity-corrected value to be used [22].

2.2. Multi-target measurement precision

We evaluated the measurement precision from the Allan deviations of the ranging data d_1, d_2 and d_3. All targets were stationary, and the combs were independently repetition frequency

Optics EXPRESS

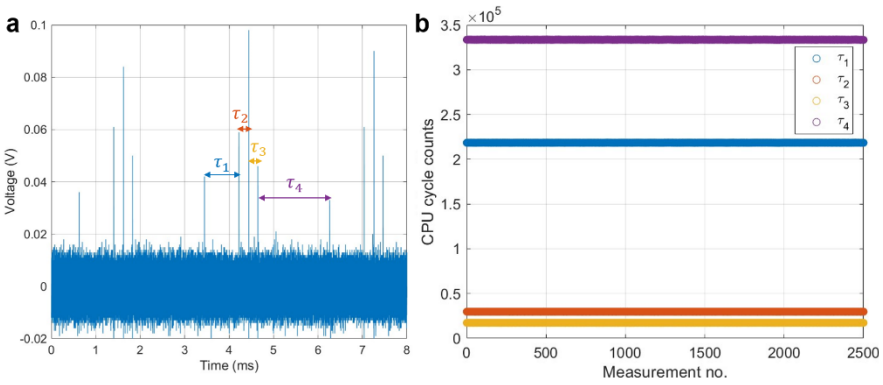

Fig. 2. (a) Oscilloscope trace of the optical cross-correlation signal over approximately three measurement cycles. Delays $\tau_1 - \tau_4$ are the timing gaps measured by the microcontroller. The cross-correlation peak heights vary for the three targets due to small differences in the alignment of the beams. (b) Raw data collected by the microcontroller plotted in Matlab.

locked to enforce Δf_{rep} = 1 kHz. The output power from the probe comb was 40 mW, meaning approximately 12 mW was incident on each target. The output power from the LO comb was 12 mW. The ranging data used for the Allan deviations are presented in Fig. 3(a). The blue data show single-shot measurements recorded every 1 ms, while the red data are the same measurements with 10 ms of averaging applied. The measured distances to the three targets are 38.65 cm ± 52 µm, 49.37 cm ± 61 µm, and 54.91 cm ± 65 µm, where statistical uncertainties are expressed as the standard deviation of the data. The Allan deviation of the calculated distance values are presented in Fig. 3(b) and show single-shot measurement precisions of 57.0 µm, 66.6 µm and 70.9 µm for the results in Fig. 3(a), respectively, aligning closely with the standard deviations of each of the entire data sets. We can conclude from these values that ranging to the first target has better precision than to the second target, and ranging to the second target has better precision than to the third target. The reduction in precision for subsequent targets is most likely caused by the uncertainty introduced by measuring multiple timing intervals. Despite this slight degradation for subsequent targets, averaging is effective in providing sub-micron precision. The Allan deviation data in Fig. 3(b) show that averaging for two seconds improves the precisions to 255 nm, 197 nm, and 254 nm, which are in fact indistinguishable within the uncertainty of the Allan deviation calculation (error bars, Fig. 3(b)). The measurement precision would be improved if all measurements were made relative to the first reference pulse, which can be arranged using suitable timing electronics.

Figure 3(b) also shows the Allan deviation of ranging data collected for free-running repetition frequencies (i.e., $f_{rep,pr}$ and $f_{rep,LO}$ were not locked). The precisions are 57.1 µm, 66.7 µm, and 71.0 µm which approximately match the single-shot precisions of measurements made while locking the repetition frequencies. However, with time-averaging the measurement precisions plateau around 1 µm for averaging times above 100 ms, with the precisions after two seconds of averaging being 1.32 µm, 1.35 µm and 1.39 µm. These results suggest that it is sufficient to leave the combs free-running when minimal averaging is used. However, locking the repetition rates ensures consistent signals and provides greatest precision when averaging is applied.

The data presented in Fig. 3(b) exhibit lower measurement precision in comparison with our original two-photon dual-comb LiDAR publication [12]. This results from multiple changes made to the system, including the use of a different Si APD and Schmitt trigger, different oscillator cavity lengths and EDFA fibre lengths, and operation at Δf_{rep} =1 kHz, whereas previous data were

Optics EXPRESS

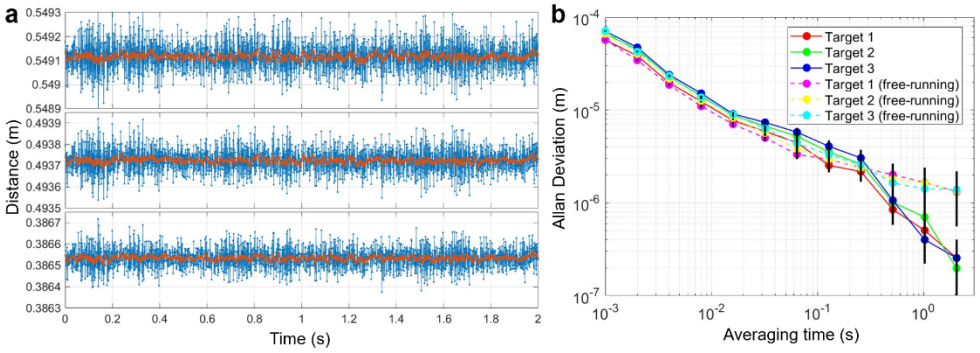

Fig. 3. (a) Simultaneous ranging to stationary retroreflectors. Blue data show single-shot measurements (1 ms), while red data are the same measurement with 10 ms of averaging. (b) Allan deviation of simultaneously collected ranging data to Targets 1-3, collected while the repetition frequencies of the combs were locked to enforce Δf_{rep} = 1 kHz. Co-plotted is the Allan deviation of simultaneous ranging data to Targets 1-3 with free-running combs.

collected for 4 kHz and 2 kHz. The nonlinear dependence of the DCR measurement precision on Δf_{rep} has been reported on by Wu *et al.* [23,24].

2.3. Simultaneous ranging to three dynamic targets

We demonstrated simultaneous ranging to three dynamic targets by mounting the target retroreflectors on loudspeakers and driving each with an independent signal generator. Figure 4(a) shows one of these retroreflectors mounted using a 3D-printed adaptor onto the front of a loudspeaker, which itself is held inside a 3D-printed mount.

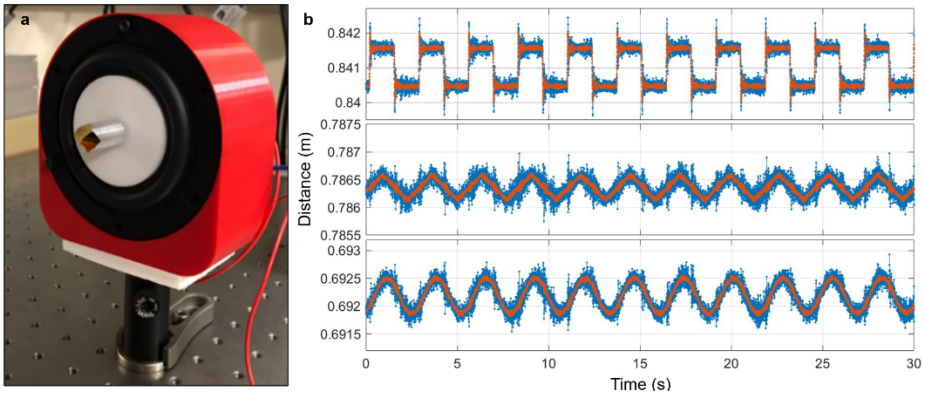

Fig. 4. (a) Dynamic targets were created by mounting each retroreflector target on a loudspeaker and driving the speaker with a signal generator. (b) Instantaneous ranging data to retroreflectors driven at 1 Hz with 10 V peak-to-peak amplitude by a sine, saw-tooth, and square-wave signal. The blue data are single-shot measurements (1 ms); the red data are the blue data with 10 ms of averaging applied.

Figure 4(b) shows ranging to three retroreflectors over a measurement period of 30 s. The blue data are single-shot measurements (1 ms), while the red data are the same measurements with 10 ms averaging. The targets were driven by sine, saw-tooth, and square-wave signals with 1 Hz frequency and 10 V peak-to-peak amplitude. The measurement shows how two-photon dual-comb LiDAR resolves the overshoot of Target 3 in response to the square-wave drive signal,

Optics EXPRESS

reflecting the true mechanical motion caused by the sudden acceleration and deceleration of the retroreflector. Disturbances in the sine and saw-tooth motions align with the square-wave frequency, suggesting two-photon dual-comb LiDAR is able to resolve vibrations in the targets caused by environmental coupling. These features vanished when the square-wave signal was removed and persisted when the square-wave target reflector was blocked, implying that they were not caused by electrical signal cross-talk, but instead were true measurements of the vibration resulting from mechanical coupling of the square-wave motion through the optical table.

3. Simultaneous range and pose measurements

3.1. Conceptual framework

The multi-target ranging technique described above can be used to make simultaneous range and pose measurements. Consider the arrangement in Fig. 5(a), where probe pulses in three parallel beams travelling along the $-z$ direction are incident on three retroreflectors, configured in an L-shaped orientation, suitable for making differential measurements of retroreflector pairs rotating around orthogonal pitch and yaw axes. After retroreflection, the probe pulses are gated by the LO pulses to produce dual-comb cross-correlations which are decoded using Eq. (1) to provide the absolute distances of the retroreflectors from the reference optic, z_i (i =1, 2 or 3).

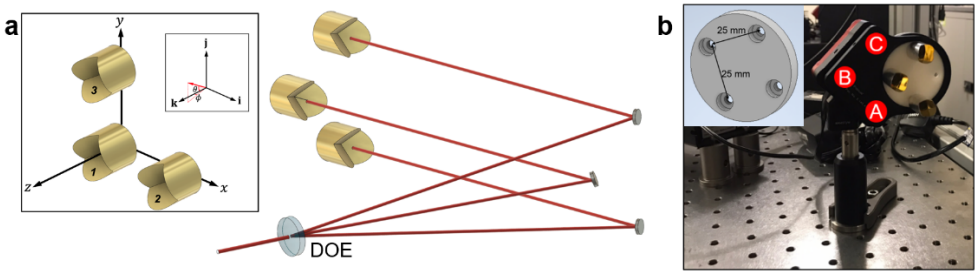

Fig. 5. (a) Mirror geometry used to reshape three vertically distributed beams emerging from the DOE into an L-shape oriented at 45°. Inset: Cartesian coordinate frame defining the retroreflector positions, where i, j and k are unit vectors parallel to the x, y and z axes respectively. (b) Picomotor stage holding the retroreflectors under investigation. Inset: Model of the 3D printed adaptor used to define the retroreflectors into an exact L-shape with a baseline of l = 25 mm.

The initial retroreflector distances define a Cartesian frame and the angular origin such that the three retroreflectors lie in the xy plane at locations $r_1 = (0, 0, 0)$, $r_2 = (l, 0, 0)$ and $r_3 = (0, l, 0)$, where l is the separation between adjacent retroreflectors. The retroreflectors are rigidly connected so that changes along the z axis in their absolute distances can be interpreted as pitch (θ) and yaw (ϕ) angles of the entire retroreflector assembly.

Accordingly, a small change of Δz_i ($\ll l$) modifies the retroreflector positions to be:

$$r_1 = (0, 0, \Delta z_1), \tag{2}$$

$$r_2 = (l, 0, \Delta z_2), \tag{3}$$

and

$$r_3 = (0, l, \Delta z_3). \tag{4}$$

The normal vector to the plane containing the retroreflectors is given by the vector product:

$$\mathbf{v} = (r_2 - r_1) \times (r_3 - r_1) \tag{5}$$

The initial value of this vector is $\mathbf{k}$, the unit vector along the z direction, so the angle between $\mathbf{k}$ and the projection of $\mathbf{v}$ onto the xz plane gives the yaw angle, ϕ, and the angle between $\mathbf{k}$ and

Optics EXPRESS

the projection of **v** onto the *yz* plane gives the pitch angle, θ, according to:

$$\phi = \cos^{-1}([\mathbf{v}\cdot\mathbf{i}, 0, \mathbf{v}\cdot\mathbf{k}]\cdot k/|[\mathbf{v}\cdot\mathbf{i}, 0, \mathbf{v}\cdot\mathbf{k}]|), \tag{6}$$

and

$$\theta = \cos^{-1}([0, \mathbf{v}\cdot\mathbf{j}, \mathbf{v}\cdot\mathbf{k}]\cdot\mathbf{k}/|[0, \mathbf{v}\cdot\mathbf{j}, \mathbf{v}\cdot\mathbf{k}]|). \tag{7}$$

3.2. Results and discussion

Figure 5 illustrates how the vertically distributed output beams from the DOE were reconfigured into an L-shaped geometry. The inset of Fig. 5(b) shows the AutoCAD model of a 3D printed mount which was used to hold three retroreflectors (Targets 1 to 3) in an L-shape on orthogonal baselines of lengths 25 mm × 25 mm – the mount design enforced l, the separation between retroreflectors, as 25 mm. The assembly was mounted into a Picomotor stage (New Focus 8852) with nominal linear and angular precisions of <30 nm and 0.7 µrad, which allowed incremental tuning of its pose. Two-photon dual-comb LiDAR measurements were collected between translations of the Picomotor stage.

The ranging data to the three retroreflectors were analyzed as follows. With the mount in its initial orientation (nominally perpendicular to the input beams), ranging data were collected for each retroreflector with 20 ms averaging, and these initial values were recorded as offsets to be removed from all subsequent measurements. In this way, these initial measurements defined a nominal origin in both pitch and yaw, indicated by the gray arrow parallel to the *z*-axis in Fig. 6 and corresponding to **k** in Section 3.1. Following the procedure of Section 3.1, vectors were drawn to connect the three target points to create a plane and obtain a vector normal to this surface, **v**, shown by the purple arrow. As described by Eqs. (6) and (7), the projection of **v** onto the *xz* and *yz* planes give the pitch and yaw angles. Figure 6 illustrates how the absolute retroreflector positions, r_1, r_2 and r_3, were visualized in a 3D Cartesian frame, along with the vectors **v** and **k**, and with the *x*, *y* and *z* axes showing the absolute distance coordinates of the three target retroreflectors.

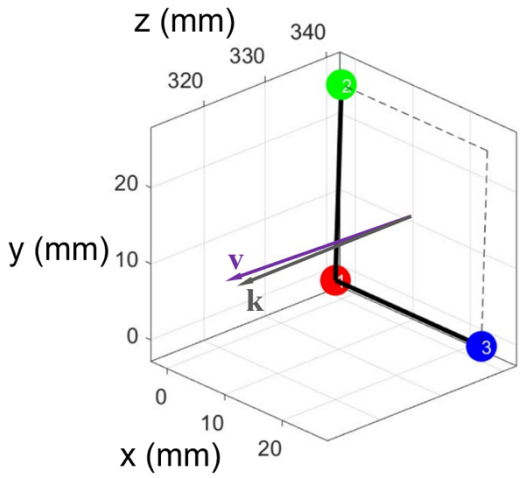

Fig. 6. Illustration of pose data analysis. The range measurements to the three targets are plotted in 3D space. Vectors drawn between the three points define a plane, whose vector normal, **v** is projected onto the *xz* and *yz* planes to obtain the pitch and yaw angles.

Figure 7 presents the measured increases in pitch and yaw for 200-step (6 µm) increments of Motors A, B and C, each over a total translation of 35,000 steps (1050 µm). The total angular

Optics EXPRESS

translation for each motor was around 3600 arcsec, which is equal to 1°. The angle measurements are presented as a proof-of-concept of the pose measurements so ground truth data were not collected. The results are organized by column for Motor A (left), Motor B (center) and Motor C (right).

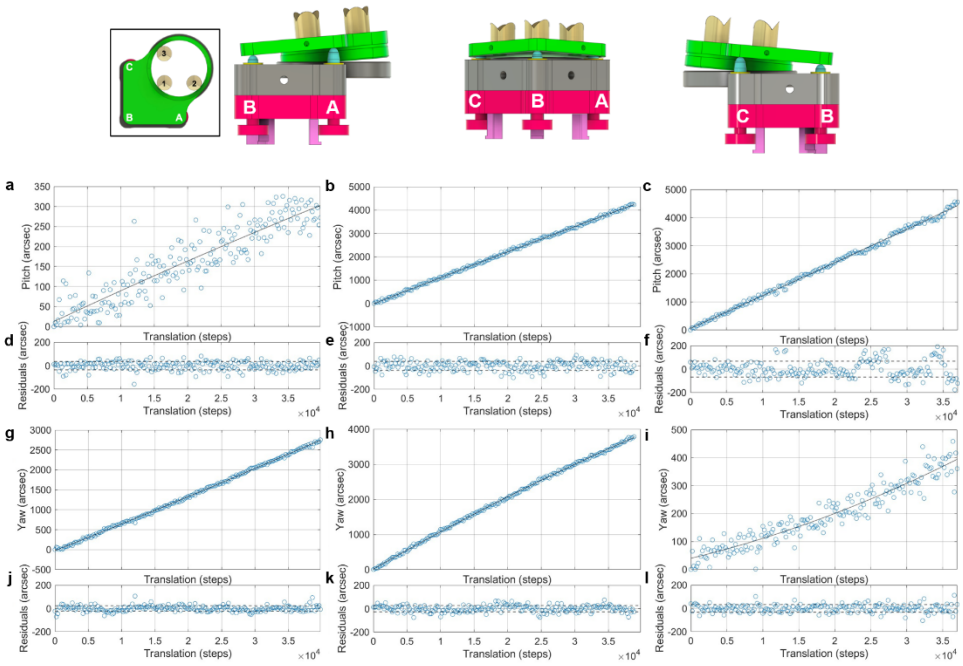

Fig. 7. Angular measurements using two-photon dual-comb LiDAR. Inset: indexing of the motors (A, B and C) and retroreflectors (1, 2 and 3) with respect to the mirror mount geometry. Columns (left to right) show increments in Motor A, Motor B and Motor C respectively. Sub-figures (a), (e) and (i), and (c), (g) and (k) show the measured changes in the pitch and yaw angles respectively, together with a low order polynomial fit to the data (black line). Sub-figures (b), (d), (f), (h), (j) and (l) plot the residuals showing the deviation of the data from these polynomial fits. The dashed lines indicate ± the standard deviation of the residuals.

In an ideal system, an angular change would be observed only for the actuated axis. However, there is a change observed in the opposite axis to the one being actuated because of a small degree of cross-talk, and misalignment between the retroreflector coordinate frame and the mirror mount coordinate frame. The rows in Fig. 7 depict the pitch (top row) and yaw (bottom row) angular data, along with a low-order polynomial fit which allows the residuals of the motion to be obtained, which are co-presented for each rotation axis. We chose to use a low order polynomial fit to separate out variance caused by the imprecision of the measurement technique from slow nonlinearities due to the geometry of the mirror mount. This approach is justified by the fact that the residuals show no bias and vary about a constant zero value. The precisions of the pitch and yaw measurements are determined from the standard deviations of the residuals. For Motor A these were 36.7 arcsec and 23.8 arcsec, respectively; for Motor B, 39.3 arcsec and 27.7 arcsec, respectively; and for Motor C, 70.0 arcsec and 31.3 arcsec, respectively. For Motor C, the pitch angle precision is worse than the angular precision of the other measurements; however, this is explained by the noticeable outliers in Fig. 7 (right column). The reason for the outliers may be imperfect alignment with the retroreflectors. However, the outliers repeat every 8000-10,000 steps of translation, and the magnitude of the outliers is around 140 arcsec. This pattern suggests

Optics EXPRESS

the outliers could be caused by a dust particle periodically moving between the drive screw and the wear face as the screw rotates.

4. Conclusions

Two-photon dual-comb LiDAR is one of the simplest implementations of DCR to date, where a trivial change from a linear to nonlinear photodiode detector enables range to be obtained from timing measurements rather than by data-intensive interferometric acquisition. Although two-photon dual-comb LiDAR reports lower precision measurements than the conventional DCR technique, the low-cost implementation, the minimal data burden, and the ability to calculate distances on-the-fly gives the technique significant practical advantages.

To date, there have been only a small number of demonstrations of DCR for multi-target measurements, and the study we have presented here now extends these to include two-photon dual-comb LiDAR. Our results have shown ranging to stationary targets with single-shot precisions of 57.1 µm, 66.6 µm and 70.9 µm at 1 ms sampling times, with only a small penalty in the measurement precision introduced when measuring multiple consecutive timing gaps between multiple target reflections. We note that this can be mitigated by using alternative timing electronics with a continuously running counter, so enabling the measurement of all timing gaps relative to the reference reflection.

In this paper we have shown demonstrations of ranging to three targets through splitting of the probe beam with a DOE. This technique could be scaled to allow many more parallel measurements by employing a DOE with higher-order diffracted outputs. The main limitation in expanding to many more targets is ensuring there is sufficient signal strength after splitting the probe beam, but an EDFA could be inserted into the return path to mitigate this loss.

We demonstrated simultaneous ranging to three dynamic targets and showed that two-photon dual-comb LiDAR recovers the motion well, even resolving the overshoot of the target driven by a square wave. No cross-talk was observed between the three measurements.

Finally, we demonstrated simultaneous range and pose measurements by ranging to three points on a rigid-body target, whose pose was adjusted by remotely controlling individual motors in a precision mirror mount to induce linear changes in pitch and yaw. The approach yields range, pitch, and yaw simultaneously and we obtained precisions as high as 27.1 arcsec for retroreflectors on a 25 mm baseline using data recorded at 1 kHz and with 20 ms averaging. The results can be compared to [16], which used a similar methodology to calculate target pose via multiple ranging measurements. Their reported ranging precision was 0.936 µm in 0.5 ms averaging time and this permitted angular precisions of 5.289 arcsec. Our angular precisions are around 5× lower, but this is unsurprising considering our ranging precision is also an order of magnitude lower. The system discussed in [16] includes high-bandwidth digitization and post-processing of the signal which is known to provide higher precisions. We are therefore satisfied with the level of precision we have achieved, considering our simpler time-stamp implementation.

The speed, simplicity of implementation and ease of data handling demonstrated in multi-target two-photon dual-comb LiDAR measurements makes the approach attractive for a wide range of static and dynamic industrial metrology applications.

Funding. The Royal Academy of Engineering (RCSRF2223-1678); Renishaw; Engineering and Physical Sciences Research Council (EP/N002547/1, EP/P006930/1).

Disclosures. The authors declare no conflicts of interest.

Data availability. Data underlying the results presented in this paper are not publicly available at this time but may be obtained from the authors upon reasonable request.

References

1. I. Coddington, W. C. Swann, L. Nenadovic, and N. R. Newbury, "Rapid and precise absolute distance measurement s at long range," Nat. Photonics **3**(6), 351–356 (2009).

Optics EXPRESS

2. T. Mitchell, J. Sun, and D. T. Reid, "Dynamic measurements at up to 130-kHz sampling rates using Ti:sapphire dual-comb distance metrology," Opt. Express **29**(25), 42119–42126 (2021).
3. D. R. Carlson, D. D. Hickstein, D. C. Cole, S. A. Diddams, and S. B. Papp, "Dual-comb interferometry via repetition rate switching of a single frequency comb," Opt. Lett. **43**(15), 3614–3617 (2018).
4. R. Jiang, S. Zhou, and G. Wu, "Aliasing-free dual-comb ranging system based on free-running fiber lasers," Opt. Express **29**(21), 33527–33535 (2021).
5. S. Zhou, V. Le, S. Xiong, Y. Yang, N. Kai, Q. Zhou, and G. Wu, "Dual-comb spectroscopy resolved three-degree-of-freedom sensing," Photonics Res. **9**(2), 243–251 (2021).
6. C. Lin, S. Zhou, R. Zhang, and G. Wu, "Dual-comb ranging method for simultaneously measuring the refractive index and surface spacing in a multi-lens system," Opt. Express **30**(26), 46001–66009 (2022).
7. D. Hu, Z. Wu, H. Cao, Y. Shi, R. Li, H. Tian, Y. Song, and M. Hu, "Dual-comb absolute distance measurement of non-cooperative targets with a single free-running mode-locked fiber laser," Opt. Commun. **482**, 126566 (2021).
8. R. Li, X. Ren, B. Han, M. Yan, K. Huang, Y. Liang, J. Ge, and H. Zeng, "Ultra-rapid dual-comb ranging with an extended non-ambiguity range," Opt. Lett. **47**(20), 5309–5312 (2022).
9. A. Q. Anderson, E. F. Strong, S. C. Coburn, G. B. Rieker, and J. T. Gopinath, "Orbital angular momentum-based dual-comb interferometer for ranging and rotation sensing," Opt. Express **30**(12), 21195–21210 (2022).
10. Y. Liu, W. Xia, M. He, S. Cao, D. Miao, B. Lin, J. Xie, W. Yang, and J. Li, "Experimental realization and characterization of a two-colour dual-comb system for practical large-scale absolute distance measurements," Opt. Lasers Eng. **151**, 106900 (2022).
11. S. L. Camenzind, J. F. Fricke, J. Kellner, B. Willenberg, J. Pupeikis, C. R. Phillips, and U. Keller, "Dynamic and precise long-distance ranging using a free-running dual-comb laser," Opt. Express **30**(21), 37245–37260 (2022).
12. H. Wright, J. Sun, D. McKendrick, N. Weston, and D. T. Reid, "Two-photon dual-comb LiDAR," Opt. Express **29**(23), 37037–37047 (2021).
13. H. Zhang, H. Wei, X. Wu, H. Yang, and Y. Li, "Absolute distance measurement by dual-comb nonlinear asynchronous optical sampling," Opt. Express **22**(6), 6597–6604 (2014).
14. J. Wang, H. Shi, C. Wang, M. Hu, and Y. Song, "Impact of laser intensity noise on dual-comb absolute ranging precision," Sensors **22**(15), 5770 (2022).
15. D. T. Reid, W. Sibbett, J. M. Dudley, L. P. Barry, B. Thomsen, and J. D. Harvey, "Commercial semiconductor devices for two photon absorption autocorrelation of ultrashort light pulses," Appl. Opt. **37**(34), 8142–8144 (1998).
16. S. Han, Y.-J. Kim, and S.-W. Kim, "Parallel determination of absolute distances to multiple targets by time-of-flight measurement using femtosecond light pulses," Opt. Express **23**(20), 25874–25882 (2015).
17. X. Xu, H. Zhao, Y. Bi, Z. Qian, C. Liu, H. Shi, and J. Zhai, "Arbitrary distance and angle measurement by dynamic dispersive interferometry using a frequency comb," Opt. Lasers Eng. **145**, 106665 (2021).
18. X. Wang, J. Su, J. Yang, L. Miao, and T. Huang, "Modified homodyne laser interferometer based on phase modulation for simultaneously measuring displacement and angle," Appl. Opt. **60**(16), 4647–4653 (2021).
19. Y. Shimizu, H. Matsukuma, and W. Gao, "Optical angle sensor technology based on the optical frequency comb laser," Appl. Sci. **10**(11), 4047 (2020).
20. Y.-L. Chen, Y. Shimizu, J. Tamada, K. Nakamura, H. Matsukuma, X. Chen, and W. Gao, "Laser autocollimation based on an optical frequency comb for absolute angular position measurement," Precis. Eng. **54**, 284–293 (2018).
21. W. Ren, J. Cui, and J. Tan, "A three-dimensional small angle measurement system based on autocollimation method," Rev. Sci. Instrum. **93**(5), 055102 (2022).
22. P. E. Ciddor, "Refractive index of air: New equations for the visible and near infrared," Appl. Opt. **35**(9), 1566 (1996).
23. G. Wu, Q. Zhou, L. Shen, K. Ni, X. Zeng, and Y. Li, "Experimental optimization of the repetition rate difference in dual-comb ranging system," Appl. Phys. Express **7**(10), 106602 (2014).
24. G. Wu, S. Xiong, K. Ni, Z. Zhu, and Q. Zhou, "Parameter optimization of a dual-comb ranging system by using a numerical simulation method," Opt. Express **23**(25), 32044–32053 (2015).

2.25.36.138 {ts '2023-09-11 09:42:12'}